PNAS
RESEARCH ARTICLE | ENGINEERING

Precursor-mediated in situ growth of hierarchical N-doped graphene nanofibers confining nickel single atoms for CO_2 electroreduction

Huan Wang[a,1], Youzeng Li[a], Maoyu Wang[b], Shan Chen[a], Meng Yao[a], Jialei Chen[a], Xuelong Liao[a], Yiwen Zhang[c], Xuan Lu[c], Edward Matios[c], Jianmin Luo[c], Wei Zhang[a], Zhenxing Feng[b,1], Jichen Dong[d,1], Yunqi Liu[d], and Weiyang Li[c,1]

Edited by Alexis Bell, University of California, Berkeley, CA; received November 10, 2022; accepted February 14, 2023

Despite the various strategies for achieving metal–nitrogen–carbon (M–N–C) single-atom catalysts (SACs) with different microenvironments for electrochemical carbon dioxide reduction reaction (CO_2RR), the synthesis–structure–performance correlation remains elusive due to the lack of well-controlled synthetic approaches. Here, we employed Ni nanoparticles as starting materials for the direct synthesis of nickel (Ni) SACs in one spot through harvesting the interaction between metallic Ni and N atoms in the precursor during the chemical vapor deposition growth of hierarchical N-doped graphene fibers. By combining with first-principle calculations, we found that the Ni-N configuration is closely correlated to the N contents in the precursor, in which the acetonitrile with a high N/C ratio favors the formation of Ni-N_3, while the pyridine with a low N/C ratio is more likely to promote the evolution of Ni-N_2. Moreover, we revealed that the presence of N favors the formation of H-terminated edge of sp^2 carbon and consequently leads to the formation of graphene fibers consisting of vertically stacked graphene flakes, instead of the traditional growth of carbon nanotubes on Ni nanoparticles. With a high capability in balancing the *COOH formation and *CO desorption, the as-prepared hierarchical N-doped graphene nanofibers with Ni-N_3 sites exhibit a superior CO_2RR performance compared to that with Ni-N_2 and Ni-N_4 ones.

Ni single atoms | precursor mediation | direct growth | Ni-N configuration | CO_2 electroreduction

Significance

Single-atomic catalysts (SACs) represent the most promising catalyst candidates in efficiently converting carbon dioxide (CO_2) into carbon monoxide (CO). Nevertheless, the complicated synthetic routes result in uncontrolled single-atomic configurations, making it rather difficult to gain an explicit understanding on how to achieve a high CO selectivity. Herein, we present a facile approach for the direct growth of N-doped graphene fibers-supported nickel (Ni) SACs through harvesting the interaction between catalytic Ni substrate and N-related species as decomposition products of N-containing precursors. Mechanistic studies reveal a dual role of N in the morphology of graphene and coordination environment of Ni SACs. This work clarifies the significance of precursor design on the single-atomic configurations and offers an ingenious strategy for achieving SACs.

The electrocatalytic carbon dioxide reduction reaction (CO_2RR) is an intriguing approach for relieving the anthropogenic CO_2 emission while storing the intermittent renewable energy in the chemical bond of valuable chemicals and fuels (1, 2). Recent technoeconomic analyses suggest that carbon monoxide (CO) is one of the most economically viable products owing to its two-electron transfer process and appreciable market benefit (3–5). More importantly, CO is a significant one-carbon building block for producing a wide variety of long-chain compounds through the methanol synthesis and Fischer–Tropsch process. To this end, tremendous efforts have been made in exploring catalysts that are selective toward CO production over the competing hydrogen evolution reaction (HER) (6–11).

Metal–nitrogen–carbon (M–N–C) catalysts with M-N_x as active sites have emerged as promising electrocatalysts in highly efficient conversion of CO_2 into CO due to their unique electronic structure and maximum atom utilization (12–16). The prevailing synthetic strategies for M–N–C catalysts can be generally divided into two types: i) thermal evaporation/release of metal-based species and then anchoring onto the available carbon supports with N heteroatoms (17–21); ii) incorporation of metal ions through specific adsorption or space confinement into the predesigned carbon hosts or frameworks, followed by high-temperature treatment in argon/ammonia atmosphere (22–28). These approaches strongly rely on the interaction of metal with the N atoms in the N-doped carbon matrices, which are either available or been synthesized before metal implantation. Thus, the involved multistep synthetic/pyrolysis procedures are not only tedious, but also would make it rather difficult to precisely control the configuration of metal center and effectively prevent metal agglomeration at high temperatures, which could limit the CO_2RR performance (13, 14). More importantly, the fundamental understanding of the inherent synthesis–structure–performance correlation still remains elusive. In addition to preventing the metal single atoms (SAs) from agglomerating, the carbon substrate morphology can influence the exposure of active sites and the mass/charge transfer, thus contributing to the final CO_2RR performance (17, 20, 24, 29). Therefore, it is highly desirable to develop a straightforward and facile route for synthesizing well-defined M–N–C catalysts that are able to establish an explicit synthesis–structure–property–performance relationship.

Competing interest statement: The authors have patent filings to disclose. H.W. and Y. Li are inventors on the CN patent application (No. CN115433953 A) regarding the synthetic method of single atoms described in this article.

This article is a PNAS Direct Submission.

[1] To whom correspondence may be addressed. Email: huan.wang0520@nankai.edu.cn, zhenxing.feng@oregonstate.edu, dongjichen@iccas.ac.cn, or weiyang.li@dartmouth.edu.

This article contains supporting information online at https://www.pnas.org/lookup/suppl/doi:10.1073/pnas.2219043120/-/DCSupplemental.

It is well known that transition metals with unpaired 3d electrons (e.g., Ni, Co, Cu) can serve as catalytic substrates for the chemical vapor deposition (CVD) growth of nanocarbons such as carbon nanotubes (CNTs) and graphene, during which the N-containing precursor can be decomposed into C-H and C-N fragments (30, 31). The as-obtained CN_x species with rich electrons are more likely to coordinate with the transition metal, forming $M–N_x$ bonds and directly incorporating into the graphitic carbon lattices. Compared with the traditional strategies, the CVD approach with transition metal as the starting material can enable the concurrence of $M-N_x$ doping and carbon growth in one spot, which makes it possible to regulate the $M-N_x$ configurations and avoid the metal agglomeration at high temperatures. Moreover, the growth kinetics of nanocarbons can be regulated through the growth parameters (e.g., hydrogen partial pressure) (32, 33), adjusting the carbon morphology without using template. Nonetheless, there has been a lack of studies and insights into this aspect.

Based on the above rationale, we ingeniously propose a Ni-catalytic CVD growth strategy for the direct synthesis of hierarchical N-doped graphene-supported Ni SAs. We explicitly correlate the $Ni-N_x$ configurations with the N ratios in the carbon feedstock through a combination of computational and experimental analyses. It is found that the concentration of N in the precursor not only dictates the coordination number of N in $Ni-N_x$, but also impacts the morphology of the carbon skeleton in alliance with hydrogen passivation. Experimentally, we successfully realize the controlled synthesis of hierarchical N-doped graphene nanofibers-supported single-atomic $Ni-N_2$, $Ni-N_3$, and $Ni-N_4$ sites by correspondingly increasing the N/C ratio of N-containing precursor. Compared to $Ni-N_2$ and $Ni-N_4$, $Ni-N_3$ shows a higher activity and selectivity toward CO production due to a higher capability in balancing the process of *COOH intermediate formation and *CO desorption. The deep insight into the formation mechanism of Ni SACs is helpful for future design of the precursors toward the optimized configuration of SACs.

Results

Fig. 1*A* schematically illustrates the ambient-pressure CVD (APCVD) growth process of N-doped graphene-supported Ni single atoms (Ni-NG). With the merit of high abundance and high dissolubility, commercially available sodium chloride (NaCl) powder was selected as the substrate to prevent Ni agglomeration. Prior to growth, NaCl was thoroughly mixed with nickel chloride ($NiCl_2$) through a dissolution and ball-milled treatment. During the annealing process under H_2 atmosphere, the $NiCl_2$ was in situ reduced to metallic Ni nanoparticles, which are uniformly distributed on NaCl surface (*SI Appendix*, Fig. S1). To gain insight into the growth mechanism of Ni SAs, acetonitrile and pyridine with different N/C ratios were selected as N-containing precursors. Meanwhile, ethanol without N atom was also employed. Purified powder was readily achieved by dissolving the CVD product in dilute hydrochloric acid and filtrating. This approach can enable mass production and gram-scale product in a one-batch synthesis (Fig. 1*B* and *SI Appendix*, Fig. S2). Notably, the synthesis process does not involve the use of harmful chemicals, which is more ecofriendly and controllable to operate than the traditional routes.

The morphology of CVD product was examined by scanning electron microscopy (SEM) and transmission electron microscopy (TEM). As shown in Fig. 1 *C* and *D*, the nanocarbons with acetonitrile and pyridine as precursors both display hierarchical nanofibers assembled by nanosheets. In the absence of $NiCl_2$, microcubes that retain the original shapes and sizes of ball-milled NaCl templates were achieved with acetonitrile as a precursor (*SI Appendix*, Fig. S3), suggesting that the presence of metallic Ni is responsible for the hierarchical nanofiber growth. While for ethanol as a precursor, CNTs were mainly observed on NaCl/$NiCl_2$ substrate (Fig. 1*E* and *SI Appendix*, Fig. S4). These results demonstrate that the CVD growth strategy is feasible and facile in controlling the carbon morphology, as discussed later. The nanocarbons with acetonitrile, pyridine, and ethanol are denoted as the Ni-NG (acetonitrile), Ni-NG (pyridine), and Ni-CNTs (ethanol), respectively.

The well-defined diffraction spots and rings in selected-area electron diffraction (SAED) pattern indicate its highly graphitic feature but with polycrystalline nature (Fig. 1*F* and *SI Appendix*, Fig. S5), possibly due to nanodomain size of graphene nanosheets and lattice disorders. Moreover, no diffraction peaks corresponding to metallic Ni or Ni oxides in Ni-NG (acetonitrile) and Ni-NG (pyridine) samples were observed. The Raman spectra in Fig. 1*G* exhibit three characteristic peaks that can be assigned to D, G, and 2D bands, respectively. The strong G band further validates the highly graphitic feature of Ni-NG products, while the presence of D band is attributed to the structural defects and partially disordered structures of the sp^2 domains caused by N and Ni dopants, which is in good accordance with SAED patterns.

The elemental mappings of Ni-NG (acetonitrile) and Ni-NG (pyridine) obtained by energy-dispersive spectroscopy (EDS) show a homogenous spatial distribution of Ni and N (Fig. 2 *A* and *B*), indicating that the Ni-N species are spread throughout the carbon matrix. Then, aberration-corrected high-angle annular dark-field scanning transmission electron microscopy (HAADF-STEM) imaging and electron energy loss spectroscopy (EELS) technique were employed to discern the Ni dispersion in Ni-NG (acetonitrile) and Ni-NG (pyridine) at the atomic scale. Isolated bright dots along with sharp peaks at ~855.2 eV in EELS spectra visually confirm the presence of single-atomic Ni species (Fig. 2 *C–E*). Notably, no Ni clusters or nanoparticles were observed. The XRD patterns of Ni-NG (acetonitrile) and Ni-NG (pyridine) samples in Fig. 2*F* both show two distinct peaks centered at around 26° and 43° that can be ascribed to the plane (002) and (100) of graphitic carbon, respectively. No characteristic peaks can be assigned to crystalline Ni species in the samples of Ni-NG (acetonitrile) and Ni-NG (pyridine). While the Ni-CNTs (ethanol) display obvious peaks associated with Ni metal after repeated acid washing (*SI Appendix*, Fig. S6), possibly due to the carbon layers' coating on Ni surface that prevents acid penetration. The sharp contrast indicates that the hierarchical structure is beneficial for electrolyte contact, which can facilitate mass transfer in the CO_2RR. The Ni content in Ni-NG (acetonitrile) and Ni-NG (pyridine) was calculated to be ~4.15 wt% and ~3.91 wt% by inductively coupled plasma atomic emission spectroscopy, respectively (*SI Appendix*, Table S1). These results verify that the direct CVD growth on metallic Ni with N-containing precursors can enable the formation of single-atomic Ni sites that are uniformly dispersed onto the hierarchical N-doped carbon lattice.

X-ray photoelectron spectroscopy (XPS) was performed to determine the chemical composition and valence states of single-atomic Ni in Ni-NG (acetonitrile) and Ni-NG (pyridine). The high-resolution N 1s XPS spectra of the two samples both reveal three kinds of N species, including pyridinic N, Ni-N, and graphitic N, suggesting the interaction between Ni and N atoms (Fig. 3 *A* and *B*). Accordingly, the Ni 2p peaks of Ni-NG (pyridine) and Ni-NG (acetonitrile) are both located between Ni^0 and Ni^{2+}, indicative of the ionic $Ni^{\delta+}$ ($0 < \delta < 2$) state in Ni-NG. Comparatively, no XPS signals related to N was detected in Ni-CNTs (ethanol), and the Ni species are a combination of Ni^0 and Ni^{2+} (*SI Appendix*, Fig. S7),

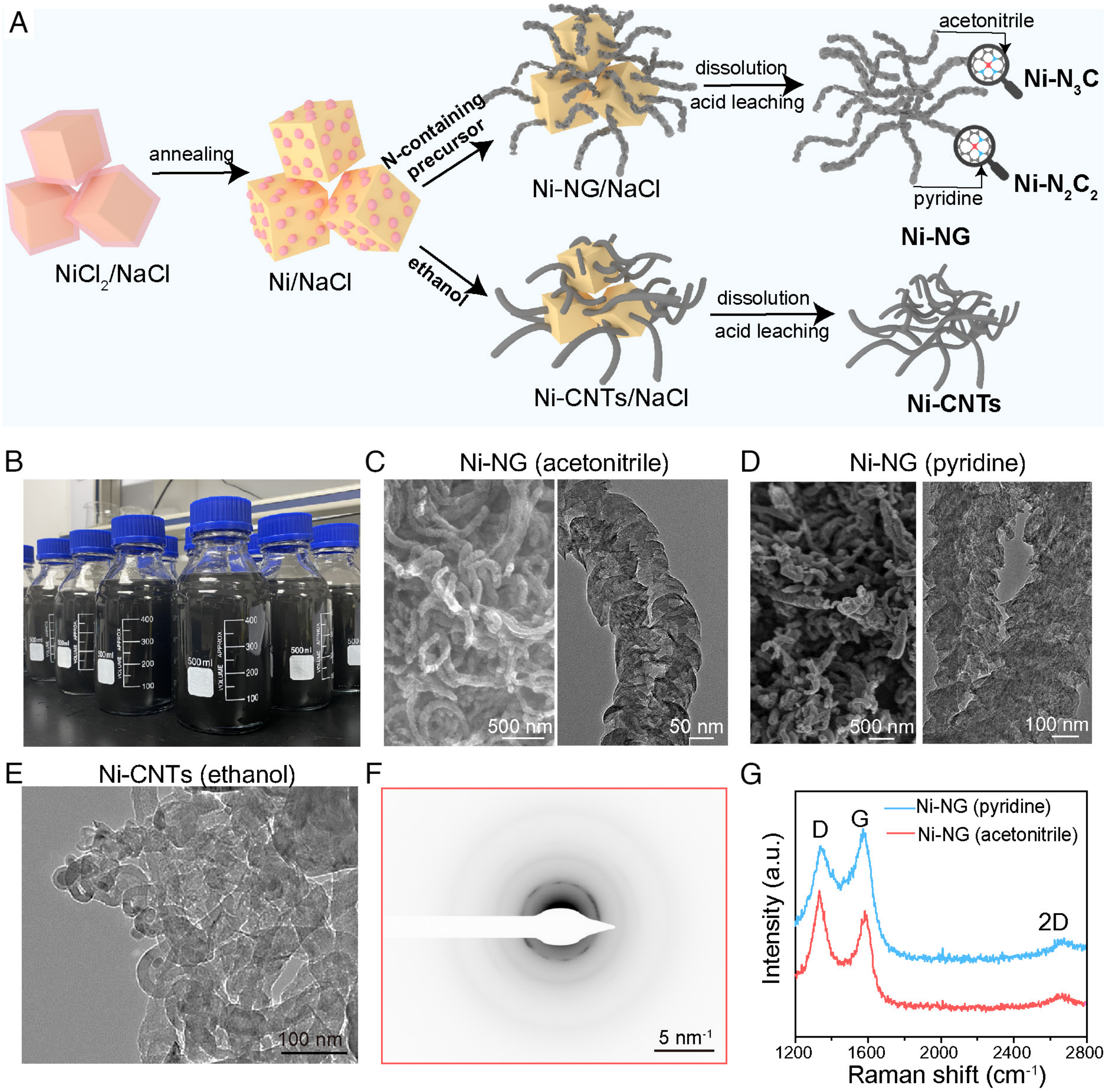

Fig. 1. Synthesis and characterizations of hierarchical N-doped graphene nanofibers-confining Ni single atoms. (*A*) Schematic of APCVD growth on NiCl$_2$/NaCl substrate with different precursors including acetonitrile, pyridine, and ethanol. (*B*) Batch production of Ni-NG aqueous solution. SEM (*Left*) and TEM (*Right*) images of Ni-NG with (*C*) acetonitrile and (*D*) pyridine as precursors, respectively. (*E*) TEM image of CNTs with ethanol as a precursor. (*F*) SAED pattern of an individual graphene nanosheet from Ni-NG (acetonitrile). (*G*) Raman spectra of Ni-NG (acetonitrile) and Ni-NG (pyridine).

largely due to the absence of Ni-N. These strongly validate that the N-containing precursors play a determining role in the formation of single-atomic Ni and Ni-N configurations.

The electronic structure of single-atomic Ni was further studied by X-ray absorption near-edge spectroscopy (XANES) and extended X-ray absorption fine structure (EXAFS) spectroscopy (34–36). As shown in Fig. 3 *C* and *D*, the absorption edges of Ni species in Ni-NG (pyridine) and Ni-NG (acetonitrile) both positively shift compared to Ni foil and are close to Ni (II) phthalocyanine (NiPc), indicating the positively charged states of Ni species (37). The Fourier-transformed (FT) Ni K-edge EXAFS profile of Ni-NG (acetonitrile) and Ni-NG (pyridine) in Fig. 3 *E* and *F* shows a prominent peak at 1.35 Å and 1.38 Å, respectively, falling near Ni-N scattering path in the first coordination shell for Ni-PC at ~1.47 Å, which can be attributed to Ni-C or Ni-N contributions. No apparent peaks assigned to Ni–Ni bonding at ~2.15 Å was observed, affirming the absence of Ni nanoparticles or Ni clusters.

To further differentiate the coordination numbers around Ni sites in Ni-NG (acetonitrile) and Ni-NG (pyridine), the EXAFS spectra were subjected to wavelet transform (WT) analysis for high-resolution information in both R and *k* spaces (38, 39). As revealed by the WT-EXAFS contour plots in Fig. 3*G*, the Ni-NG (acetonitrile) exhibits a single-intensity maximum at 3.8 Å^{-1} assigned to Ni-N, which situates between Ni-NG (pyridine) at 3.4 Å^{-1} and NiPc at 4.2 Å^{-1}. This implies that the N coordination numbers around Ni sites follow the decreasing order: NiPc > Ni-NG (acetonitrile) > Ni-NG (pyridine). According to the EXAFS fitting results (Fig. 3 *E* and *F* and *SI Appendix*, Fig. S8 and Table S2), it can be concluded that the local structure of single-atomic Ni in Ni-NG (acetonitrile) consists of three N atoms and one C atom, while the one in Ni-NG (pyridine) is coordinated with two N atoms and two C atoms. Therefore, the configuration of Ni sites in Ni-NG (acetonitrile) and Ni-NG (pyridine) is proposed to be Ni-N$_3$C and Ni-N$_2$C$_2$, respectively. The above results ascertain our hypothesis that engineering of N content of

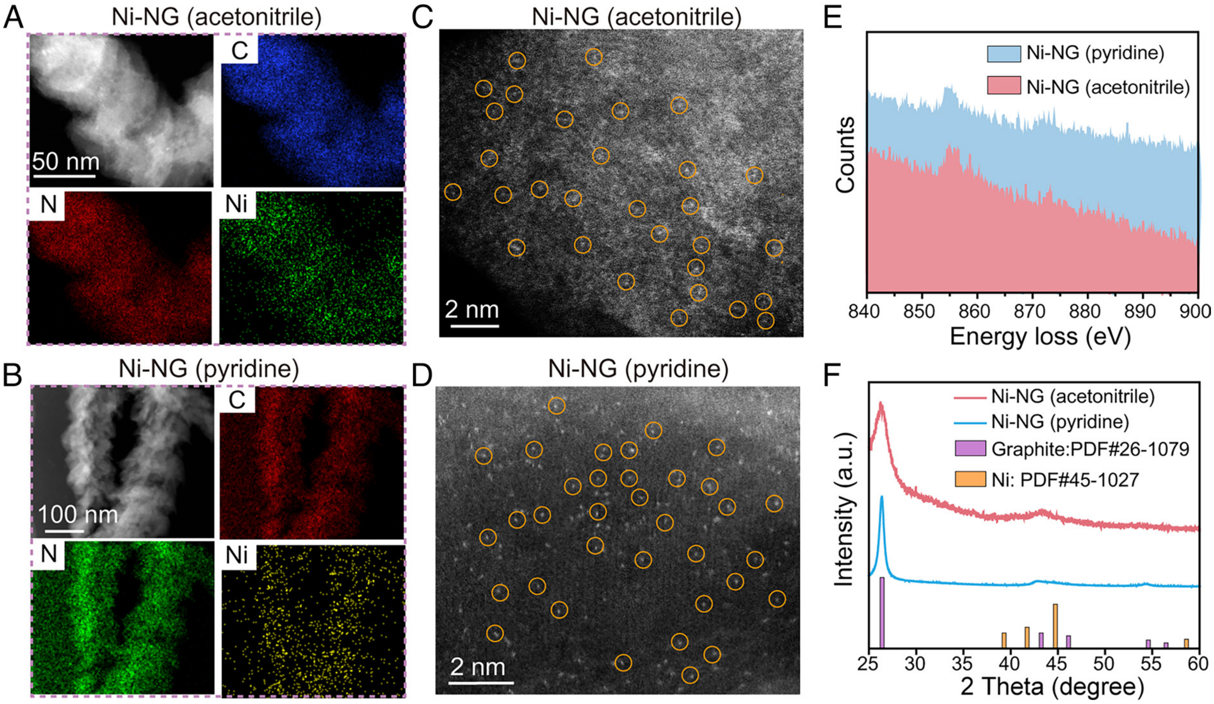

Fig. 2. Characterizations of Ni single atoms. TEM image and EDS elemental mappings of C, N, and Ni in (*A*) Ni-NG (acetonitrile) and (*B*) Ni-NG (pyridine). HAADF-STEM image of (*C*) Ni-NG (acetonitrile) and (*D*) Ni-NG (pyridine). Some representative Ni single atoms are marked with yellow circles. (*E*) EELS spectra of Ni-NG (acetonitrile) and Ni-NG (pyridine). (*F*) XRD patterns of Ni-NG (acetonitrile) and Ni-NG (pyridine).

precursors can enable the tailored microenvironments of isolated Ni sites.

To elucidate the effect of N-containing precursor on the Ni-N_x configuration, density functional theory (DFT) calculations were performed to reveal the stability of various Ni coordination environments. As shown in Fig. 4*A*, eight types of Ni single atoms with different structures are employed, namely, Ni-N_4, Ni-N_3, Ni-N_3C, Ni-N_2C_2-I, Ni-N_2C_2-II, Ni-N_2C_2-III, Ni-NC_3, and Ni-C_4. The Ni-N_3 structure is constructed by substituting four neighboring carbon atoms in the graphene sp^2 network by one Ni and three N atoms. Due to the much larger atomic radius of Ni than C, the single Ni atom in the Ni-N_3 structure shows an out-of-plane distortion. The rest seven kinds of structures are constructed by placing a Ni atom to a double-vacancy site of graphene and then replacing 0-4 C atoms around the Ni atom by N, and no visible out-of-plane distortion is observed in these structures. Their relative stabilities are assessed by their formation energies, as defined by the equation below:

$$E_F = E_T - N_C\varepsilon_C - N_N\mu_N - \varepsilon_{Ni}, \qquad [1]$$

where E_T is the total energy of the Ni coordination structure; ε_C and ε_{Ni} represent the energy of a C in perfect graphene sheet and Ni atom in Ni crystal, respectively; μ_N is the chemical potential of N; and N_C and N_{Ni} represent the number of C and Ni atoms, respectively. Fig. 4*B* shows the formation energy profiles of these eight types of Ni coordination structures as a function of μ_N. In our calculation, the energy of one N atom adsorbed on Ni surface is −8.6 eV and therefore, a reasonable range of μ_N from −10 to −8 eV is chosen. It can be seen that the Ni-N_2C_2-I structure is most stable under a low μ_N, suggesting that a low concentration of N in the synthesis environment favors the formation of NiN_2C_2-I. With the increase of μ_N, the formation energies of both Ni-N_3C and Ni-N_4 become comparable to that of NiN_2C_2-I. Therefore, with the increase of N concentration in the synthesis environment, Ni-N_3C and Ni-N_4 will be gradually formed. We have estimated the proportion of each Ni coordination structure ρ_i as a function of μ_N using the equation below:

$$\rho_i = \frac{e^{-E_{F\_i}/kT}}{\sum_i e^{-E_{F\_i}/kT}}, \qquad [2]$$

where *k*, *T*, and *i* are Boltzmann constant, temperature, and structure index, respectively. As shown in Fig. 4*C*, under low μ_N, Ni-N_2C_2-I is the dominant structure. With the increase of μ_N to −9.23 eV, the proportion of Ni-N_3C gradually increases. These results suggest that the coordination structure of Ni single atoms embedded in graphene can be effectively tuned by the concentration of N in the synthesis environment. That is, the pyridine with a low N/C ratio favors the formation of Ni-N_2C_2-I, and the acetonitrile precursor with a high N/C ratio is beneficial for Ni-N_3C production. Guided by the theoretical calculations, we further increased the N/C ratio of precursor by mixing ethylenediamine ($C_2H_8N_2$) and acetonitrile (C_2H_3N) with a volume ratio of 2:1, which is defined as Ni-NG (ethylenediamine). As expected, hierarchical graphene nanofibers confining Ni-N_4 configurations were successfully obtained with atomic Ni content of 4.30 wt%, as shown in Figure *SI Appendix*, Figs. S9 and S10 and Tables S1 and S2, indicating the great potential of our precursor-mediated growth strategy in adjusting the microenvironment of single atoms.

Then, DFT calculations were conducted to understand the growth mode of hierarchical N-doped graphene nanofibers. It has been well acknowledged that Ni nanoparticles can serve as catalysts for synthesis of CNTs, as schematically shown in the upper panel of Fig. 4*D*. During the growth of a CNT on a Ni nanoparticle, its root (edge) is strongly attached to the surface of Ni nanoparticle. Our previous studies have also shown that the edge of CNT can also be passivated by hydrogen (H) (32), leading to a weak binding between the CNT edge and catalyst surface and thus a termination of the CNT growth (33). Consequently, a graphitic

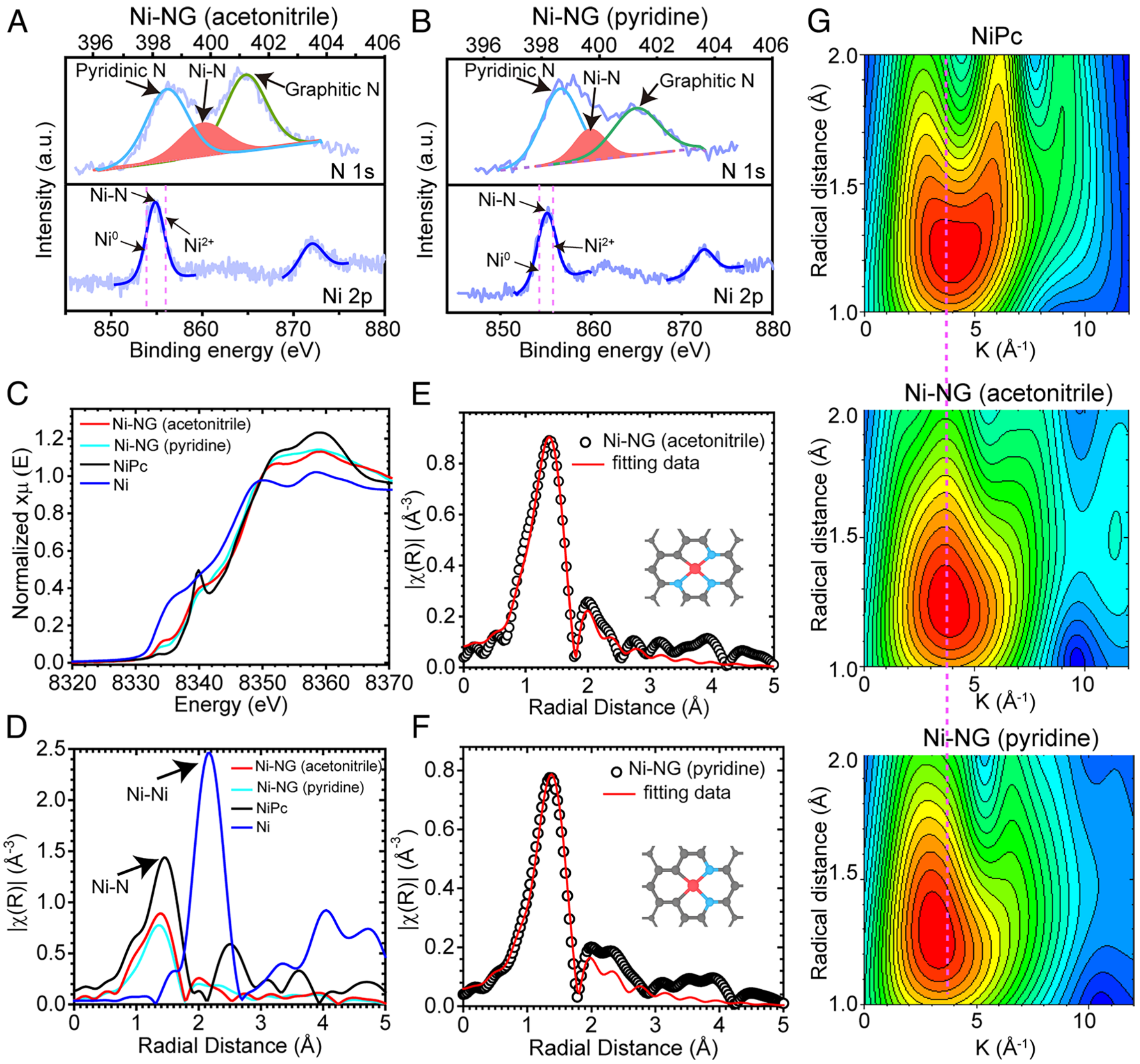

Fig. 3. Characterizations of Ni coordination environment in Ni-N-G. XPS spectrum of N 1s (*Top*) and Ni 2p (*Bottom*) for (*A*) Ni-NG (acetonitrile) and (*B*) Ni-NG (pyridine), respectively. (*C*) Ni K-edge XANES spectra. (*D*) k^3-weighted χ(k) function of the EXAFS spectra. EXAFS fitting curve for Ni sites in (*E*) Ni-NG (acetonitrile) and (*F*) Ni-NG (pyridine). *Insets* are the proposed configurations. (*G*) Wavelet transform (WT) EXAFS (R space) of NiPc (*Top*), Ni-NG (*Middle*), and Ni-NG (*Bottom*).

fiber consisting of graphene nanoflakes connected by weak van der Waals interaction might be formed (*Lower* panel of Fig. 4*D*). To form such a structure, the stability of H-terminated CNT edge needs to be more stable than that of the Ni-terminated CNT edge. We calculated the formation energies of H-terminated and Ni-terminated CNT edges (see *SI Appendix*, Fig. S11 for calculation details). As shown in Fig. 4*E*, the formation energy of H-terminated CNT edge decreases exponentially with the partial pressure of H_2 in synthesis environment, while the formation energy of Ni-terminated CNT edge increases linearly with the increase of Ni concentration on the surface of Ni catalyst. Based on the growth condition that the partial pressure of H_2 is ~5 KPa, the formation energy of H-terminated CNT edge is calculated to be 0.32 eV nm^{-1}. Therefore, by increasing the line concentration of Ni on the surface of Ni nanoparticle to >0.5 nm^{-1}, the CNT growth mode (Ni-terminated CNT edge) will be changed to the graphitic fiber growth mode (H-terminated CNT edge). This is realized by the N-containing precursor used in our experiments.

The electrochemical CO_2 reduction performance of the prepared samples was evaluated in a gas-tight three-electrode H-type cell containing 0.5 M potassium bicarbonate ($KHCO_3$). All potentials are measured with reference to RHE (reversible hydrogen electrode) except noted. The Faradaic efficiency of gas products was analyzed by online gas chromatography (GC). As shown in the linear sweep voltammetry (LSV) curves in Fig. 5*A*, the Ni-NG (acetonitrile) shows the highest current density and most positive onset reduction potential as compared to Ni-NG (pyridine) and Ni-NG (ethylenediamine), suggesting the more active nature of Ni-N_3C than Ni-N_2C_2 and Ni-N_4. Moreover, the three kinds of sample recorded in the CO_2-saturated $KHCO_3$ solution are all higher than that of Ni-NG (acetonitrile) in Ar-saturated electrolyte, indicating that Ni-N_4, Ni-N_3C, and Ni-N_2C_2 atomic sites are all more active for CO_2RR than HER. This hypothesis can be further validated by CO_2RR selectivity. As shown in Fig. 5*B*, the Ni-NG (acetonitrile) achieves a higher Faradaic efficiency for CO production (FE_{CO}) in a more positive voltage range with respect to Ni-NG (pyridine) and Ni-NG (ethylenediamine). The CO selectivity in Ni-NG (acetonitrile) reaches a maximum Faradaic efficiency of 91.7% at −0.74 V, where the Ni-NG (pyridine) exhibits a quite low FE_{CO} of ~31.7%. As the potential negatively shifted, the CO selectivity in Ni-NG (pyridine) gradually increases and finally reaches a maximum FE_{CO} of 85.6% at −0.81 V. On sharp contrast, the CO selectivity in Ni-NG (ethylenediamine) is lower than that of Ni-NG (acetonitrile) but higher than that of Ni-NG (pyridine) over the relatively low potential range. At −0.77 V, the maximum FE_{CO} in Ni-NG (ethylenediamine) reaches 72.6%.

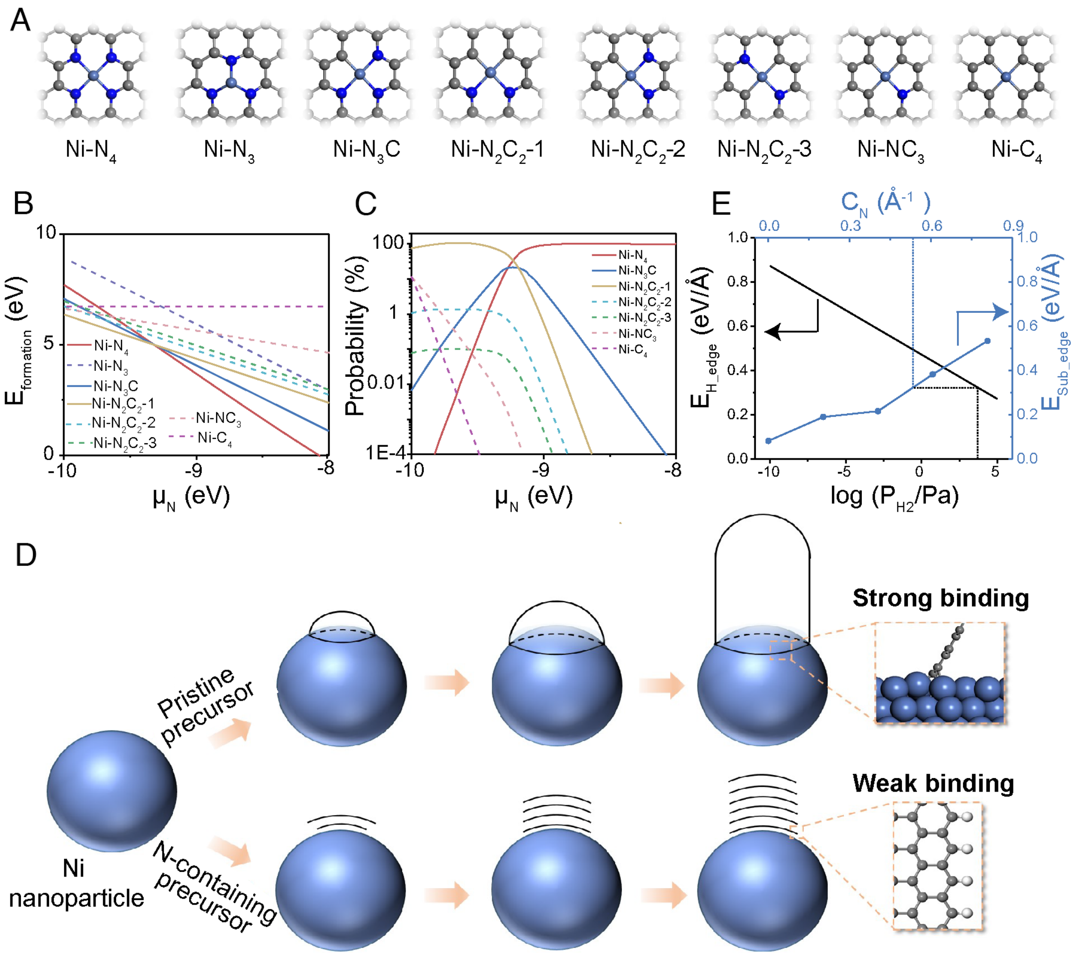

Fig. 4. Theoretical modeling on the stabilities of various Ni single-atom coordination structures in sp^2 carbon and their formation mechanism. (*A* and *B*) Structure and formation energies of various types of Ni coordination in sp^2 carbon. (*C*) Relative proportions of various Ni coordination structures as a function of the chemical potential of N and μ_N. (*D*) Schematics showing the CVD growth mechanisms of CNT and/or graphitic fibers on Ni nanoparticles. (*E*) Formation energies of H-terminated and Ni-terminated CNT edges as functions of H_2 partial pressure and N concentration in precursor on Ni nanoparticle.

Accordingly, the Ni-NG (acetonitrile) exhibits the highest partial current density of CO (j_{CO}) over the entire potential range (*SI Appendix*, Fig. S12), suggesting the superior CO_2RR performance of Ni-NG (acetonitrile) as compared to Ni-NG (pyridine) and Ni-NG (ethylenediamine). In comparison, H_2 is the major reduction product for Ni-CNTs with negligible CO production (Fig. 5*B* and *SI Appendix*, Figs. S13 and S14), indicating the pivotal role of single-atomic Ni in catalyzing the conversion of CO_2 into CO.

Furthermore, the double-layer capacitances (C_{dl}) of all the samples were obtained through comparing the cyclic voltammetry (CV) curves with the value for bare carbon cloth (*SI Appendix*, Fig. S15). Apparently, the C_{dl} of Ni-NG (acetonitrile), Ni-NG (pyridine), and Ni-NG (ethylenediamine) are very close, which are all ~5 times higher than that of Ni-CNT, indicating that the hierarchical graphene-like structures feature a high electrochemical active surface area, which facilitates fast charge transfer during the CO_2RR. Moreover, the Tafel slope of Ni-NG (acetonitrile) is 110.1 mV dec^{-1} and much lower than that of Ni-NG (pyridine) (197.8 mV dec^{-1}) and Ni-NG (ethylenediamine) (247.7 mV dec^{-1}), elucidating the superior kinetics of $Ni\text{-}N_3C$ for CO_2RR compared to $Ni\text{-}N_2C_2$ and $Ni\text{-}N_4$. Notably, our direct growth strategy for $Ni\text{-}N_3C$ catalysts exhibits a comparable Tafel slope with those of reported $Ni\text{-}N_x$ catalysts at a relatively high current density range (10, 20, 23, 40–44).

The morphological and structural analysis of the Ni SAs after CO_2RR is essential to illustrate the stability of the catalysts. To this end, we carried out a series of postmortem analyses on the sample of Ni-NG (acetonitrile), Ni-NG (pyridine), and Ni-NG (ethylenediamine). As shown in *SI Appendix*, Fig. S16, the Ni-NG (acetonitrile) can well preserve its hierarchical morphology with uniform spatial distribution of Ni and N throughout the carbon matrix. Moreover, the HAADF-STEM image reveals the isolated bright dots along with sharp peaks at ~855.0 eV in EELS spectra, indicating the existence of Ni SAs. No observable Ni clusters or nanoparticles indicates the structural stability of graphene-supported $Ni\text{-}N_3$ species. This can be further confirmed by the Ni 2p peaks that are both located between Ni^0 and Ni^{2+} before and after CO_2RR (*SI Appendix*, Fig. S17), where no Ni^0 or Ni^{2+} is detected. Likewise, the Ni-NG (pyridine) and Ni-NG (ethylenediamine) also remain at the original morphology, single-atomic dispersion, and ionic $Ni^{\delta+}$ ($0 < \delta < 2$), as shown in *SI Appendix*, Figs. S18 and S19.

To elucidate the effect of Ni coordination configuration on CO_2RR behavior, we calculated the free energy diagram of electrochemical CO_2 reduction into CO by DFT calculations, and the corresponding pathway is presented in Fig. 5*D*. For the first intermediate *COOH formation, the free energy changes on the three kinds of sites are all endergonic and increase in the following order of $Ni\text{-}N_4$ (1.47 eV) > $Ni\text{-}N_3C$ (0.89 eV) ≥ $Ni\text{-}N_2C_2$ (0.87

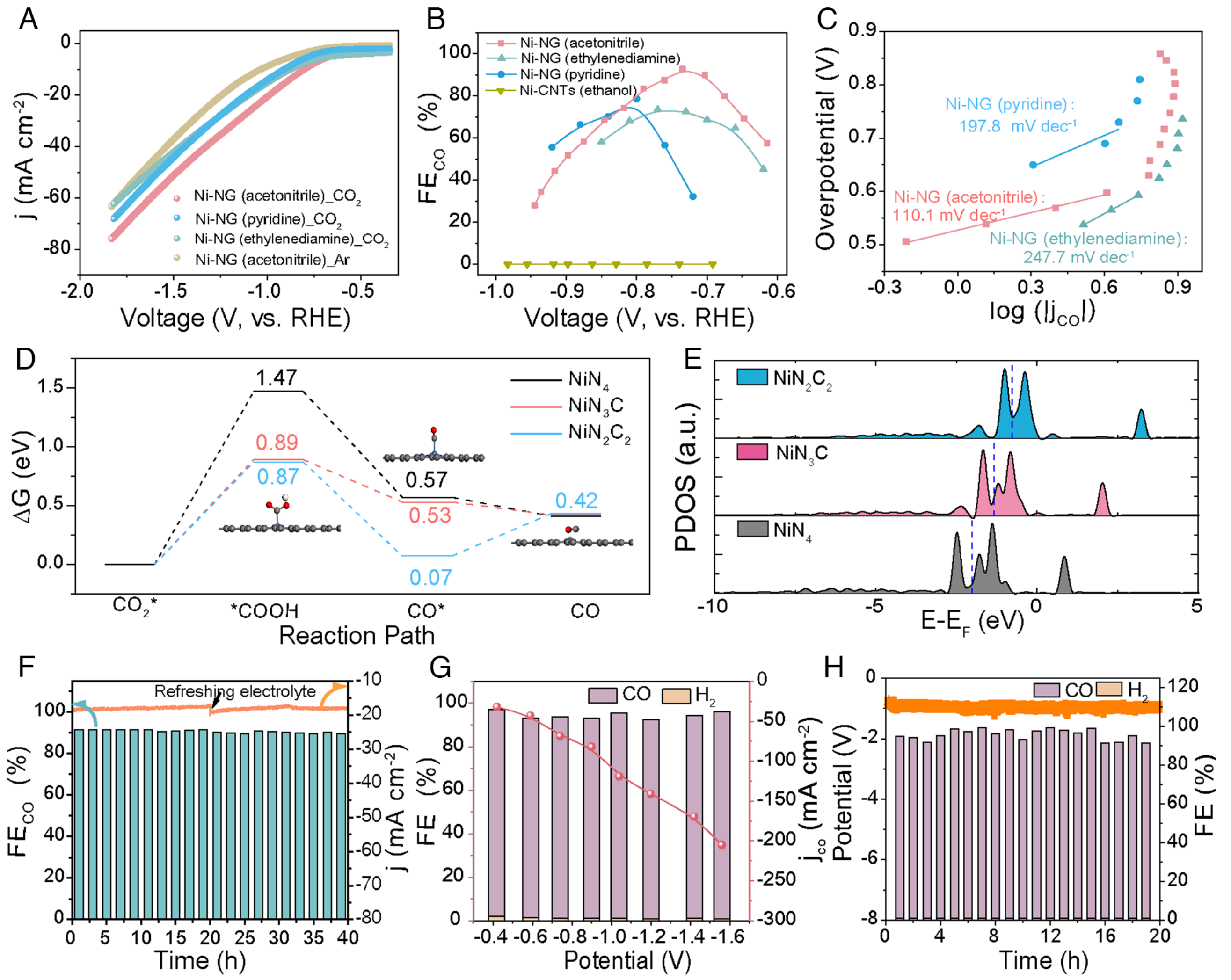

Fig. 5. Electrochemical CO_2 reduction measurements. (*A*) LSV curves acquired in CO_2-saturated or Ar-saturated 0.5 M $KHCO_3$ solution on Ni-NG (acetonitrile), Ni-NG (pyridine), and Ni-NG (ethylenediamine). (*B*) Faradaic efficiencies of CO on Ni-NG (acetonitrile), Ni-NG (pyridine), Ni-NG (ethylenediamine), and Ni-CNTs at different applied potentials. (*C*) Tafel plots of the CO partial current density for the Ni-NG (acetonitrile), Ni-NG (pyridine), and Ni-NG (ethylenediamine). (*D*) Free energy diagram of CO_2RR pathways on Ni-N_4, Ni-N_3C, and NiN_2C_2 sites. (*E*) Projected density of states for the d orbitals of Ni in NiN_4, NiN_3C, and NiN_2C_2. The d band centers are denoted by blue dash lines. (*F*) Stability of Ni-NG (acetonitrile) at −0.78 V in the H-type cell. (*G*) Faradaic efficiency of CO and H_2 (*Left*), partial current density of CO (*Right*), and (*H*) stability test at 100 mA cm^{-2} on Ni-NG (acetonitrile) in the flow cell.

eV). The lower free energy changes for both Ni-N_3C and Ni-N_2C_2 suggest that they have superior ability for CO_2 activation and protonation than the common Ni-N_4. The *COOH is then hydrogenated to transform into *CO and this process is exothermic on all the three kinds of sites. However, desorption of *CO from Ni-N_2C_2 to produce CO gas is endergonic (with a binding energy of 0.35 eV), indicating that Ni-N_2C_2 sites can be easily poisoned by *CO. In contrast, the free energy change for *CO desorption from Ni-N_3C sites is negative (with a binding energy of −0.11 eV), suggesting the spontaneous CO desorption. To further elucidate the adsorption of CO on NiN_4, NiN_3C, and NiN_2C_2, we calculated the d band center of Ni in NiN_4, NiN_3C, and NiN_2C_2 sites, respectively. As shown in Fig. 5*E*, the d band centers of Ni in NiN_4, NiN_3C, and NiN_2C_2 sites are −2.03 eV, −1.33 eV, and −0.77 eV, respectively. Since a higher d band center represents a higher chemical activity of the Ni atom, the binding energy of CO on the NiN_2C_2 should be largest, and then followed by those on the NiN_3C and NiN_4 sites. This result is consistent with our calculations on the free energy changes.

Furthermore, we conducted in situ electrochemical attenuated total reflection Fourier-transform infrared spectroscopy to monitor the *CO intermediate on Ni-N_2C_2, Ni-N_3C, and Ni-N_4 at different potentials in CO_2-saturated 0.5 M $KHCO_3$ solution. Compared to Ni-N_3C and Ni-N_4, the Ni-N_2C_2 sites exhibit an obvious peak at ~1,910 to 1,940 cm^{-1} that can be assigned to *CO at a lower potential (*SI Appendix*, Fig. S20), validating our calculation results that the *CO is difficult to release from Ni-N_2C_2 sites, thus requiring a high overpotential to promote CO desorption. By contrast, the Ni-NG (ethylenediamine) shows a negligible *CO peak especially at lower potentials, matching well with the conclusion that of a large energy barrier is acquired to produce *COOH intermediate on Ni-N_4 sites. Moreover, the Ni-NG (pyridine) and the Ni-NG (acetonitrile) both show bands redshift as potential decreases, as expected from the vibrational Stark effect (45). Thus, the Ni-NG (acetonitrile) with Ni-N_3C sites shows the best CO_2RR performance due to a higher capability in balancing the *COOH formation and *CO desorption.

Long-term stability of the catalysts is also a critical factor to evaluate the CO_2RR performance. To this end, we monitored the CO and H_2 evolution for 40 h of continuous catalysis. As depicted in Fig. 5*F*, the current density is relatively stable with a consistently high FE (CO) of above 90%, indicating the good pristine stability of Ni-NG (acetonitrile). Owing to the low solubility of CO_2 in aqueous electrolyte, the current density is severely restricted by the low mass transfer. To mitigate this issue, we performed CO_2RR in a flow cell equipped with gas-diffusion electrodes (GDEs) in 1 M KOH electrolyte. As shown in Fig. 5*G*, the Ni-NG (acetonitrile) delivers a FE_{CO} higher than 95 % at different potentials from −0.4 V to −1.6 V with the maximum partial current density for CO (j_{CO}) approaching 200 mA cm^{-2}, which is much higher than that in the H-type cell. Moreover, the Faradic efficiency of CO achieved in the Ni-NG (acetonitrile) remains stable (>90%) after 20 h of continuous electrocatalysis at a current density of 100 mA cm^{-2} (Fig. 5*H*). The high Faradic efficiency of CO and good stability at high current densities demonstrate the practical application of Ni-NG (acetonitrile) toward CO production.

Discussion

In summary, we have proposed an efficient strategy for the direct growth of N-doped hierarchical graphene nanofibers-supported Ni single atoms, which allows to establish an explicit synthesis–structure–property–performance correlation. A combined study of theoretical calculations and experimental characterizations reveals that the N content in the precursor plays a critical role in regulating the formation of hierarchical graphene nanofibers catalyzed by Ni nanoparticles, the microenvironment of single-atomic Ni sites, and the final electrocatalytic CO_2RR performance. By selecting an appropriate N-containing precursor with a higher N/C ratio, we realize the scalable synthesis of hierarchical N-doped graphene nanofibers confining Ni-N_3C sites in one spot, which is found to facilitate *COOH formation and the release of *CO intermediates. The as-prepared Ni-NG catalysts with Ni-N_3 sites achieve a high CO Faradaic efficiency of 91.7% at −0.74 V, much superior to that with Ni-N_2 ones. This work provides a perspective to design the coordination environment of single-atomic sites.

Materials and Methods

Synthesis of Hierarchical N-Doped Graphene Nanofibers Confining Ni Atoms. 40 g commercial sodium chloride (NaCl) crystal (99.5%, EMD Millipore Corporation Shanghai Aladdin Biochemical Technology Co., Ltd.) was first mixed with 1 g commercial nickel chloride ($NiCl_2$) salt and then dissolved in deionized water, followed by evaporation, drying, and high-energy mechanical milling treatment, forming $NiCl_2$/NaCl mixture. Then, graphene growth was carried out in a home-built ambient-pressure chemical vapor deposition (CVD) system. The $NiCl_2$/NaCl mixture was placed in the hot center of the furnace (Lindberg/Blue M) equipped with 1-inch-diameter quartz tube. The system was repeatedly purged with 50 sccm hydrogen (H_2) and 450 sccm argon (Ar) to remove air. Then, the furnace was heated up to 700 to 720 °C with the same flow at ambient pressure, wherein the $NiCl_2$ was reduced to metallic Ni nanoparticles that catalyze the graphene growth and embed into the graphene lattice. After maintaining for 10 min, the N-doped graphene-confining Ni single atoms (Ni-NG) were initiated through introduction of nitrogen (N)-containing compound by carrier gas. Acetonitrile (99%, Shanghai Macklin Biochemical Co., Ltd.) and pyridine (99%, Sinopharm Chemical Reagent Co., Ltd.) were employed as the precursors to achieve Ni-NG (acetonitrile) and Ni-NG (pyridine), which was predominated with Ni-N_3 and Ni-N_2 configuration, respectively. The mixture of liquid ethylenediamine and acetonitrile with a volume ratio of 2:1 was used as the precursor for Ni-N_4 configuration. Before growth, liquid precursor was stored in a stainless-steel container. After 0.5 to 2 h of growth, the furnace was cooled down to room temperature under the protection of 50 sccm H_2 and 450 sccm Ar. Then, the Ni-NG-covered NaCl/Ni powders were immersed in deionized water with diluent hydrochloric acid overnight to dissolve NaCl/Ni substrates. Finally, the Ni-NG powders were collected via filtration process, repetitively washed with water, and lyophilized. For the growth of Ni-CNTs, ethanol was employed as the precursor with the same growth procedure.

Characterizations. Scanning electron microscope (SEM) images were obtained using FEI Scios2 SEM and JSM-7500F. Transmission electron microscope (TEM) images, energy-dispersive spectroscopy (EDS) mappings, and corresponding selected area electron diffraction (SAED) were performed on a Talos F200X G2. The aberration-corrected high-angle annular dark-field scanning TEM (HAADF-STEM) images and electron energy loss spectroscopy (EELS) were collected by JEOL NEOARM 200F with a probe corrector. Raman spectra were collected on a Horiba HR800 Raman system with 532 nm laser wavelength. X-ray photoelectron spectroscopy (XPS) analysis was conducted on Thermo ESCALAB 250XI with Al K Alpha (photon energy = 1,486.6 eV) anode mono X-ray source. X-ray diffraction (XRD) measurements were performed on a Smart Lab 9 KW X-ray diffractometer equipped with a Cu-target X-ray tube (λ = 0.154 nm) operated at 150 mA and 40 kV. Part of X-ray absorption fine spectroscopy measurements were carried out using Beamline of TPS44A1 in National Synchrotron Radiation Research Center, Taiwan, and the rest XANES and EXAFS experiments were performed at beamline 2-2 at Stanford Synchrotron Radiation Light source of SLAC National Accelerator Laboratory. A Lytle detector was used to collect Ni K-edge fluorescence signal. All XAS data analyses were performed with Athena to extract XANES information, and the model-based EXAFS fitting was performed with Artemis. In-situ electrochemical attenuated total reflection-Fourier-transform infrared spectroscopy (FTIR) experiments were carried out on Thermofisher Scientific Nicolet iS50 FTIR spectrometer. The spectra were collected every 30 s at a constant potential with a wavelength of 4 cm^{-1}.

Electrochemical Measurements. The CO_2 reduction experiments were carried out in a gas-tight H-type cell separated by anion exchange membrane with 0.5 M potassium bicarbonate ($KHCO_3$) as electrolyte, which was connected to an electrochemical workstation (CHI 660E). 10 mg as-prepared catalyst was dispersed in 2 mL ethanol containing 20 μL 5 wt% Nafion under stirring to form a homogenous slurry and then casted onto carbon fiber paper or gas-diffusion electrode (GDE), followed by drying in a vacuum oven, serving as the working electrode. Saturated calomel electrode (SCE) and platinum (Pt) mesh were used as reference electrode and counter electrode, respectively. All potentials were converted to reversible hydrogen electrode (RHE) based on the following equation:

$$E\,(\text{vs. RHE}) = E\,(\text{vs. SCE}) + 0.244\ \text{V} + 0.0591 \times \text{pH}. \qquad [\mathbf{3}]$$

Before each test, CO_2 gas was continuously fed to the cathodic compartment with a flow rate of 30 sccm for 0.5 h to remove the air and form CO_2-saturated 0.5 M $KHCO_3$ solution. All the potentials were recorded with a constant iR-correction excepted noted. For the flow cell measurements in a custom-designed flow cell reactor, Ag/AgCl was employed as the reference electrode. The catholyte was 1 M KOH. All potentials were converted to RHE according to the following equation:

$$E\,(\text{vs. RHE}) = E\,(\text{vs. Ag/AgCl}) + 0.197\ \text{V} + 0.0591\ \text{V} \times \text{pH}. \qquad [\mathbf{4}]$$

Linear sweep voltammetry (LSV) spectra were collected at a scan rate of 10 mV·s^{-1} under Ar-saturated or CO_2-saturated 0.5 M $KHCO_3$ electrolyte. The electrochemical impedance spectroscopy measurements were performed by applying an AC voltage with 5 mV amplitude in a frequency range from 100 kHz to 0.01 Hz. The gas-phase products were detected by a gas chromatograph (GC-2014) equipped with a flame ionization detector (FID) and a thermal conductivity detector, which were used to quantify the concentration of carbon monoxide (CO) and hydrogen (H_2), respectively. The gas concentration (x_i) was achieved by the peak area and the corresponding calibration curve. The Faradaic efficiency for CO and H_2 product was calculated as follows:

$$FE = x_i * \textit{flow rate} * \frac{2F\,p_0}{RT * j} * 100\%, \qquad [\mathbf{5}]$$

where p_0 = 1 atm, *F* is the Faradaic constant, *R* is the gas constant, *T* is the detection temperature, *j* is the current density at selected potentials, and flow rate = 30 sccm.

Theoretical Calculation Details. Density functional theory (DFT) calculations were performed via the Vienna ab initio simulation Package (46, 47). The Perdew–Burke–Ernzerhof generalized gradient approximation was employed to treat the exchange-correlation effect (48). The interaction between the ionic cores and valence electrons was described by the projected augmented wave method (49). To account for the weak van der Waals interaction between graphene and Ni, the DFT-D2 method was used (50). An energy cutoff of 400 eV was chosen for the plane wave basis. The distance between adjacent K-points in the Monkhorst–Pack scheme is set to be 0.03 $Å^{-1}$ (51).

To calculate the formation energy of Ni-terminated CNT edge in the presence of N, a Ni (111) slab consisting of three atomic layers was constructed to model the surface of Ni nanoparticle, and a graphene nanoribbon along zigzag direction was used to attach to the Ni (111) surface (*SI Appendix*, Fig. S11). The formation energy E_F of the Ni-terminated CNT edge is defined by:

$$E_F = E_{F\_ZZ} + E_b, \qquad [6]$$

where E_{F_ZZ} is the formation energy of a bare graphene zigzag edge as referred to a perfect graphene, and E_b is the binding energy between the graphene nanoribbon and the Ni (111) surface.

The relative free energy profiles for the CO_2RR are calculated by:

$$\Delta G_{COOH} = G_{COOH} - G_{CO_2} - \mu_H, \qquad [7]$$

$$\Delta G_{CO^*} = G_{CO^*} - G_{CO_2} + \mu_{H_2O} - 2\mu_H, \qquad [8]$$

$$\Delta G_{CO} = G_{CO} - G_{CO^*}, \qquad [9]$$

where G_{COOH}, G_{CO_2}, and G_{CO^*} represent the free energy of COOH, CO_2, and CO adsorbed on single atom Ni site, respectively; G_{CO} is the free energy of desorbed CO; μ_H and μ_{H2O} are the free energies of one H atom in H_2 and H_2O under standard condition, respectively; G_{COOH}, G_{CO_2}, and G_{CO^*} are calculated by $G = E_T + \sum_i \left[\frac{1}{2}\hbar w_i + k_B T ln(1 - e^{-\hbar w_i / k_B T})\right]$. The free energy of desorbed CO is calculated by the harmonic oscillation approximation method for gas molecules.

Data, Materials, and Software Availability. All study data are included in the article and/or *SI Appendix*.

ACKNOWLEDGMENTS. This work was supported by the National Natural Science Foundation of China (no. 22105107, 22173109, and 52072185), Ministry of Science and Technology of China (2021YFA1201900), and Fundamental Research Funds for the Central Universities (No. 020/C029201005). W.L. acknowledges the start-up funds at Thayer School of Engineering, Dartmouth College. H.W. acknowledges the Young Elite Scientists Sponsorship Program by Tianjin. J.D. and Y.Liu acknowledge the Chinese Academy of Sciences and the Strategic Priority Research Program of the Chinese Academy of Sciences (XDB30000000). Z.F. acknowledges the funding support from U.S. NSF (CBET-1949870 and CBET-2016192) for related X-ray absorption spectroscopy measurements. Use of the Stanford Synchrotron Radiation Lightsource, SLAC National Accelerator Laboratory, is supported by the U.S. Department of Energy, Office of Science, Office of Basic Energy Sciences under contract no. DE-AC02-76SF00515. The theoretical calculations were carried out on TianHe-1(A) at the National Supercomputer Center at Tianjin. This research used resources of the Analysis Platform of New Matter Structure at Nankai University.

Author affiliations: [a]Key Laboratory of Advanced Energy Materials Chemistry (Ministry of Education), Renewable Energy Conversion and Storage Center, College of Chemistry, Nankai University, Tianjin 300071, China; [b]School of Chemical, Biological, and Environmental Engineering, Oregon State University, Corvallis, OR 97331; [c]Thayer School of Engineering, Dartmouth College, Hanover, NH 03755; and [d]Beijing National Laboratory for Molecular Sciences, Key Laboratory of Organic Solids, Institute of Chemistry, Chinese Academy of Sciences, Beijing 100190, China

Author contributions: H.W. and W.L. designed research; H.W., Y. Li, M.W., S.C., M.Y., J.C., X. Liao, Y.Z., X. Lu, W.Z., Z.F., and J.D. performed research; H.W., Y. Li, M.W., S.C., M.Y., X. Liao, E.M., J.L., W.Z., Z.F., J.D., and Y. Liu analyzed data; and H.W., J.D. and W.L. wrote the paper.

1. S. Nitopi *et al.*, Progress and perspectives of electrochemical CO_2 reduction on copper in aqueous electrolyte. *Chem. Rev.* **119**, 7610–7672 (2019).
2. X. Tan *et al.*, Recent advances in innovative strategies for the CO_2 electroreduction reaction. *Energy Environ. Sci.* **14**, 765–780 (2021).
3. D. Xu *et al.*, Electrocatalytic CO_2 reduction towards industrial applications. *Carbon Energy* **5**, 1–27 (2022).
4. M. Jouny *et al.*, General techno-economic analysis of CO_2 electrolysis systems. *Ind. Eng. Chem. Res.* **57**, 2165–2177 (2018).
5. O. Bushuyev *et al.*, What should we make with CO_2 and how can we make it? *Joule* **2**, 825–832 (2018).
6. Y. Pan *et al.*, Design of single-atom Co–N_5 catalytic site: A robust electrocatalyst for CO_2 reduction with nearly 100% CO selectivity and remarkable stability. *J. Am. Chem. Soc.* **140**, 4218–4221 (2018).
7. J. Rosen *et al.*, Electrodeposited Zn dendrites with enhanced CO selectivity for electrocatalytic CO_2 reduction. *ACS Catal.* **5**, 4586–4591 (2015).
8. X. Li *et al.*, Exclusive Ni–N_4 sites realize near-unity CO selectivity for electrochemical CO_2 reduction. *J. Am. Chem. Soc.* **139**, 14889–14892 (2017).
9. J. Wang *et al.*, Defective bimetallic selenides for selective CO_2 electroreduction to CO. *Adv. Mater.* **34**, 2106354 (2022).
10. Z. Chen *et al.*, Amination strategy to boost CO_2 electroreduction current density of M-N/C single-atom catalysts to industrial application level. *Energy Environ. Sci.* **14**, 2349–2356 (2021).
11. W. Ge *et al.*, Dynamically formed surfactant assembly at the electrified electrode–electrolyte interface boosting CO_2 electroreduction. *J. Am. Chem. Soc.* **144**, 6613–6622 (2022).
12. J. Gu *et al.*, Atomically dispersed Fe3+ sites catalyze efficient CO2 electroreduction to CO. *Science* **364**, 1091–1094 (2019).
13. Z. Shi *et al.*, Metal-nitrogen-doped carbon materials as highly efficient catalysts: Progress and rational design. *Adv. Sci.* **7**, 2001069 (2020).
14. X. Li *et al.*, Microenvironment modulation of single-atom catalysts and their roles in electrochemical energy conversion. *Sci. Adv.* **6**, eabb6833 (2020).
15. Md. Hossain *et al.*, Reaction mechanism and kinetics for CO_2 reduction on nickel single atom catalysts from quantum mechanics. *Nat. Commun.* **11**, 2256 (2020).
16. M. Li *et al.*, Heterogeneous single-atom catalysts for electrochemical CO_2 reduction reaction. *Adv. Mater.* **32**, 2001848 (2020).
17. Y. Li *et al.*, Synthesis of N-doped highly graphitic carbon urchin-like hollow structures loaded with single-Ni atoms towards efficient CO_2 electroreduction. *Angew. Chem. Int. Ed.* **61**, e202201491 (2022).
18. S. Liu *et al.*, Chemical vapor deposition for atomically dispersed and nitrogen coordinated single metal site catalysts. *Angew. Chem. Int. Ed.* **59**, 21698–21705 (2020).
19. J. Yang *et al.*, In situ thermal atomization to convert supported nickel nanoparticles into surface-bound nickel single-atom catalysts. *Angew. Chem. Int. Ed.* **57**, 14095–14100 (2018).
20. Y. Gang *et al.*, One-step chemical vapor deposition synthesis of hierarchical Ni and N co-doped carbon nanosheet/nanotube hybrids for efficient electrochemical CO_2 reduction at commercially viable current densities. *ACS Catal.* **11**, 10333–10344 (2021).
21. Y. Qu, Direct transformation of bulk copper into copper single sites via emitting and trapping of atoms. *Nat. Catal.* **1**, 781–786 (2018).
22. H. Yang *et al.*, A universal ligand mediated method for large scale synthesis of transition metal single atom catalysts. *Nat. Commun.* **10**, 4585 (2019).
23. X. Rong *et al.*, Controlled synthesis of a vacancy-defect single-atom catalyst for boosting CO_2 Electroreduction. *Angew. Chem. Int. Ed.* **59**, 1961–1965 (2020).
24. H. Yang *et al.*, Carbon dioxide electroreduction on single-atom nickel decorated carbon membranes with industry compatible current densities. *Nat. Commun.* **11**, 593 (2020).
25. H. Yang *et al.*, Atomically dispersed Ni (I) as the active site for electrochemical CO_2 reduction. *Nat. Energy* **3**, 140–147 (2018).
26. T. Zheng *et al.*, Large-scale and highly selective CO_2 electrocatalytic reduction on nickel single-atom catalyst. *Joule* **3**, 265–278 (2019).
27. Y. Zhang *et al.*, Rational fabrication of low-coordinate single-atom Ni electrocatalysts by MOFs for highly selective CO_2 reduction. *Angew. Chem. Int. Ed.* **60**, 7607–7611 (2021).
28. L. Zhang *et al.*, Graphene defects trap atomic Ni species for hydrogen and oxygen evolution reactions. *Chem.* **4**, 285–297 (2018).
29. F. Pan *et al.*, Atomically dispersed iron-nitrogen sites on hierarchically mesoporous carbon nanotube and graphene nanoribbon networks for CO_2 reduction. *ACS Nano.* **14**, 5506–5516 (2020).
30. L. Lin *et al.*, Bridging the gap between reality and ideal in chemical vapor deposition growth of graphene. *Chem. Rev.* **118**, 9281–9343 (2018).
31. L. Qian *et al.*, Building a bridge for carbon nanotubes from nanoscale structure to macroscopic application. *J. Am. Chem. Soc.* **143**, 18805–18819 (2021).
32. J. Dong *et al.*, Formation mechanism of overlapping grain boundaries in graphene chemical vapor deposition growth. *Chem. Sci.* **8**, 2209–2214 (2017).
33. F. Ding *et al.*, The importance of strong carbon-metal adhesion for catalytic nucleation of single-walled carbon nanotubes. *Nano Lett.* **8**, 463–468 (2008).
34. M. Wang, Z. Feng, Interfacial processes in electrochemical energy systems. *Chem. Commun.* **57**, 10453–10468 (2021).
35. M. Wang, Z. Feng, Pitfalls in x-ray absorption spectroscopy analysis and interpretation: A practical guide for general users. current opinion in electrochemistry. *Curr. Opin. Electrochem.* **30**, 100803 (2021).
36. M. Wang *et al.*, In situ x-ray absorption spectroscopy studies of nanoscale electrocatalysts. *Nanomicro Lett.* **11**, 47 (2019).
37. X. Zhang *et al.*, Molecular engineering of dispersed nickel phthalocyanines on carbon nanotubes for selective CO_2 reduction. *Nat. Energy* **5**, 684–692 (2020).
38. H. Funke *et al.*, Wavelet analysis of extended X-ray absorption fine structure data. *Phys. Rev. B* **71**, 094110 (2005).
39. H. Funke *et al.*, A new FEFF-based wavelet for EXAFS data analysis. *J. Synchrotron Rad.* **14**, 426–432 (2007).
40. Y. Gong *et al.*, Regulating the coordination environment of MOF-templated single-atom nickel electrocatalysts for boosting CO_2 reduction. *Angew. Chem. Int. Ed.* **59**, 2705–2709 (2020).
41. K. Jiang *et al.*, Isolated Ni single atoms in graphene nanosheets for high-performance CO_2 reduction. *Energy Environ. Sci.* **11**, 893–903 (2018).
42. W. Bi *et al.*, Surface immobilization of transition metal ions on nitrogen-doped graphene realizing high-efficient and selective CO_2 reduction. *Adv. Mater.* **30**, 1706617 (2018).
43. Y. Li *et al.*, Loading single-Ni atoms on assembled hollow N-rich carbon plates for efficient CO_2 electroreduction. *Adv. Mater.* **34**, 2105204 (2022).
44. H. Guo *et al.*, Ni single-atom sites supported on carbon aerogel for highly efficient electroreduction of carbon dioxide with industrial current densities. *eScience* **2**, 295–303 (2022).
45. X. Chang *et al.*, Understanding the complementarities of surface-enhanced infrared and raman spectroscopies in CO adsorption and electrochemical reduction. *Nat. Commun.* **13**, 2656 (2022).

46. G. Kresse, J. Hafner, Ab initio molecular dynamics for open-shell transition metals. *Phys. Rev. B* **48**, 13115–13118 (1993).
47. G. Kresse, J. Furthmüller, Efficiency of ab-initio total energy calculations for metals and semiconductors using a plane-wave basis set. *Comput. Mater. Sci.* **6**, 15–50 (1996).
48. S. Grimme, Semiempirical GGA-type density functional constructed with a long-range dispersion correction. *J. Coput. Chem.* **27**, 1787–1799 (2006).
49. G. Kresse, D. Joubert, From ultrasoft pseudopotentials to the projector augmented-wave method. *Phys. Rev. B* **59**, 1758–1775 (1999).
50. J. P. Perdew, B. Kieron, E. Matthias, Generalized gradient approximation made simple. *Phys. Rev. Lett.* **77**, 3865–3868 (1996).
51. H. J. Monkhorst, J. D. Pack, Special points for brillouin-zone integrations. *Phys. Rev. B* **13**, 5188–5192 (1976).